Published in "Spectrochimica Acta Part B: Atomic Spectroscopy, 2010
doi: 10.1016/j.sab.2010.02.013" which should be cited to refer to this work.

Depth profiles of Al impurities implanted in Si wafers determined by means of the high resolution grazing emission x-ray fluorescence technique

Y. Kayser*[,a], W. Cao[a], J.-Cl. Dousse[a], J. Hoszowska[a], P. Jagodzinski[b], M. Kavcic[c], A. Kubala-Kukus[b], S. Nowak[a], M. Pajek[b], J. Szlachetko[d]

[a] *Department of Physics, Universtiy of Fribourg, CH-1700 Fribourg, Switzerland*
[b] *Institute of Physics, Jan Kochanowski University, 25-406 Kielce, Poland*
[c] *J. Stefan Institute, SI-1000, Ljubljana, Slovenia*
[d] *European Synchrotron Radiation Facility (ESRF), F-38043 Grenoble, France*

Abstract

The synchrotron based high resolution grazing emission x-ray fluorescence (GEXRF) technique is used to extract the distribution of Al ions which were implanted with a dose of 10^{16} atoms/cm^2 in Si wafers with different energies ranging between 1 and 100 keV. In this purpose an angular scan around the critical angle was made. In addition special efforts were made to improve the experimental conditions. The extracted depth distributions are compared to theoretical calculations of the depth distributions resulting from ion implantations and a good agreement was found. Ion implantation is indeed a useful tool in the semiconductor industry, especially in the production of integrated circuits and junctions. The high-resolution GEXRF technique could support further developments in this domain.

Key words:
grazing emission x-ray fluorescence (GEXRF), depth profiling, synchrotron radiation, ion implantation

1. Introduction

The usefulness of ion implantation was first discussed by Shockley in the early 1950's [1] and today it is one of the techniques of choice when it comes

*Corresponding author. E-mail address: yves.kayser@unifr.ch

up to alter near surface properties. Ion implantation is for example used in steel surface finishing [2], in order to increase the resistance towards corrosion, and in the domain of semiconductors [3], its most successful application, to fabricate integrated circuits: electrical properties of selected areas of the semiconductor device are modified by bombarding these areas with energized ions. In fact the process of ion implantation consists in accelerating ions of some element onto a given substrate. The ions penetrate the substrate and loose their kinetic energy during nuclear collisions and electron capture processes until they come to rest. The final distribution of the ions depends on their initial kinetic energy, the kind of ions and the kind of substrate. For kinetic energies in the keV range, typical mean ion penetration depths are on the nanometre scale.

An alternative technique to ion implantation is dopant diffusion which presents the advantage that several wafers can be treated simultaneously with. However ion implantation allows for a better control over the implantation parameters, i.e. the final shape of the distribution, the profile, and hence the reproducibility is better [3]. However, independently on the chosen implantation technique, it is necessary to control experimentally the dopant concentration profiles. This necessity becomes more and more important with shrinking device sizes. Indeed, for reasons of device-scaling, decreasing device sizes require shallower profiles and, thus, lower implantation energies. However, a shallower profile means also that the defects produced by the implantation process are confined in a narrower region. Finally the profile depends much more on the implantation conditions. Therefore an exact knowledge of dopant concentration profiles down to currently nanometre-scales is important for the semiconductor industry. There exist several well-established methods for depth-profiling which have each their advantages and drawbacks.

The most popular of all depth-profiling methods is probably SIMS which is largely used and very precise. However SIMS, besides being destructive, suffers form the formation of a so-called transient region resulting in an inaccessible region: the first 10 to 15 nm below the surface cannot be quantified, meaning that dopant distributions realized with low implantation energies cannot be recovered. RBS does not present this drawback but suffers from its rather low depth resolution and low efficiency for light elements. On the other hand techniques based on electrons like AES or XPS are quite sensitive but, due to the low mean penetration depth of electrons, they are confined to the surface and, thus, depth profiles cannot be realized for dopant distri-

butions implanted at higher energies. Besides this, a absolute quantification is quite difficult if not impossible. On the other hand TXRF and GEXRF do not suffer from the mentionned drawbacks. Quantification problems have been discussed for GEXRF in [4] and [5] resp. for implanted samples and XRF in [6]. By tuning the incidence respectively exit angles, the accessible region for measurements with TXRF and GEXRF can be changed from few nanometres to hundreds of nanometres showing that these methods have the ability to deal with a broader range of ion-implanted samples than SIMS or AES resp. XPS. TXRF has also been combined with chemical etching [7] for depth-profiling but in this case the advantage of non-destructibility is lost. TXRF and GEXRF present thus, an interesting alternative to the already known methods of depth-profiling by performing angular-dependant scans. This procedure will be more explicitly described for GEXRF in the next sections.

2. Principles of GEXRF

GEXRF is based on the same physical principle as TXRF [8] which is the refraction of x-rays due to a sudden change of the refractive index. GEXRF is therefore, like TXRF, used for the analysis of thin layers to determine their thickness and density or the quantification of trace amounts of impurities on surfaces. Both techniques profit from a low background and present good detection limits which can be enhanced by using preconcentration techniques like VPD (vapour phase decomposition). In fact a typical GEXRF setup corresponds to an inversed TXRF setup: in TXRF measurements the samples are irradiated at grazing incidence angles and the emitted fluorescence x-rays are detected at a normal direction with respect to the sample surface. In GEXRF the sample surface is irradiated at macroscopic angles and the emitted fluorescence line is detected at grazing exit angles.

The equivalence between these two geometries was first shown by [9] who used the principle of microscopic reversibility which states that grazing incidence and grazing emission type experiments provide identical results if the energies of interest are the same. If this condition is verified the depth distributions of atoms contributing to the experimental result are identical. The energy of interest for grazing incidence setups is the primary x-ray beam energy, for grazing exit experiments it is the one of the measured x-ray fluorescence line. Since the latter one is lower than the beam energy, grazing emission type experiments are generally more sensitive to the absorption of

x-rays. In addition, as it is illustrated in figure 1 for the Al-Kα line, the critical angles are higher since they depend inversely on the x-ray energy. Figure 1 shows also that the angle of interest, i.e. the incidence angle in TXRF respectively the exit angle in GEXRF, needs to be larger in grazing emission setups than in grazing incidence setups if the same extinction depth should be reached and, thus, identical sample regions should contribute to the measured intensity.

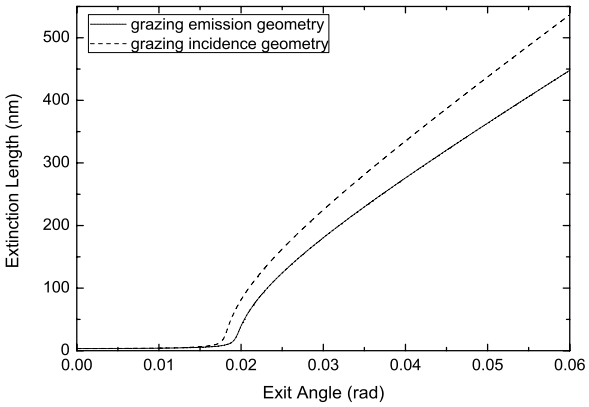

Figure 1: Evolution of the extinction length for the primary beam resp. the fluorescence line with the angle of interest which is the incidence angle for grazing incidence setups and the exit angle for grazing exit setups. The extinction length is the distance in the depth direction after which the intensity has dropped by a factor $\exp -1$ and gives an estimation of which up to which depth Al atoms contribute to the detected signal.

An advantage of TXRF setups is certainly the large solid angle of detection. In fact these large solid angles are needed for reasons of detection efficiency since the incident beam needs to be highly collimated in order to have a well defined grazing incidence angle. If a wavelength-dispersive setup is used, the fluorescence line will also be collimated, resulting in a low sensitivity of the setup [10]. Therefore, in grazing incidence setups, energy dispersive detectors mounted close to the target surface are used. However in the case of light elements, energy dispersive detectors are not very efficient and, in addition, due to the lower resolution, the fluorescence lines of neighbouring elements will at least partially overlap. This difficulties are reported

for the combination of Al and Si in [11]. On the other hand the combination of wavelength-dispersive detection setups, which are more favourable for the detection of low-Z elements, with grazing emission conditions is possible without loosing too much in detection efficiency. This allowed us to use the already existing high resolution von Hamos spectrometer of the University of Fribourg [12].

An other attractive feature of GEXRF setups is the independancy on the type of the incoming beam. Monochromatic x-rays from a synchrotron source, the Bremsstrahlung from an x-ray tube, or ionized particles like electrons and ions can be used. In addition focussed and collimated x-ray beams can be used if needed in GEXRF setups which allow performing surface scans as it is shown in [13]. Such surface scans cannot be realized with grazing incidence geometries since the incoming beam spreads over the target surface. By addressing the problem of depth-profiling it can be demonstrated that even 3D scans are possible with GEXRF setups. Other potential applications of GEXRF setups are reported in [14].

3. Measurements

The presented measurements were realized with the high resolution von Hamos crystal x-ray spectrometer of the University of Fribourg. As angular dependant measurements require a precise control over the exit angle, a new driving motor for the target holding system was installed which allows changing the exit angle with a minimum step of 0.00225°. Grazing emission conditions are realized by turning the flat target surface, mounted perpendiclarly to the dispersion plane, close enough to the detection direction defined by the Bragg angle of the ADP (101) crystal curved cylindrically ($R = 25.4$ cm) around the dispersion axis. Only x-rays hitting the crystal surface at the Bragg angle, defined by the energy of the x-rays and the lattice spacing of the crystal, can be diffracted towards the back-illuminated position-sensitive CCD detector ($1340 * 400$ pixels of $20 * 20$ μm^2 each). In this way, as shown in figure 2, a fixed target position corresponds to a given exit angle and angular dependant scans are performed by changing successively the target position. As the crystal itself sees the target only as a line-like source, the angular resolution is mainly determined by the Darwin width of the crystal. Usually slits are used to define the exit angle, but this is of no need here. The result is an increased intensity since the whole irradiated target surface can emit towards the crystal. It should however be noted, that the angular resolution

can be spoiled if the target is not mounted at 90° to the dispersion plane. For this reason, the vertical range of the CCD contributing to the result was limited.

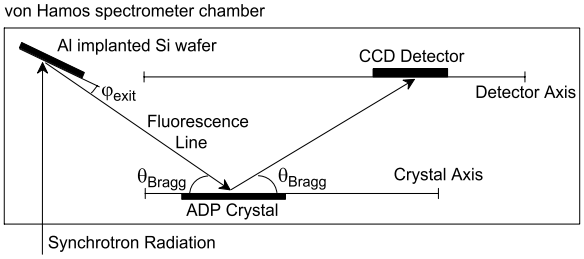

Figure 2: Illustration of how grazing emission conditions are realized with the high resolution von Hamos crystal spectrometer. The crystal is bent cylindrically around the detector axis, with a bending radius equal to the distance between the crystal and the detector axis in order to focus the diffracted x-rays onto the detector surface. Note that no slits need to be used to define an exit angle or to increase the angular resolution.

The ID21 beamline at ESRF in Grenoble was used to realize the measurements. The primary x-ray beam was delivered by a wiggler and monochromatized by two Ni/B_4C multilayers after having passed Si mirrors making an angle of 12 mrad with respect to the incident beam. Approximately $2 * 10^{12}$ photons were impinging per second on the target. The beam energy resolution was about 6 eV for the two energies of interest which were 1.582 keV for the detection of the Al-Kα line respectively 2.000 keV for the Si-Kα line. The energy selected for the excitation of the Al-Kα fluorescence line was guided by several considerations. Besides the suppression of the strong Si-Kα fluorescence line and the increased photoabsorption cross-section if an excitation energy just above the Al K-edge is chosen, this excitation energy also resulted in a considerable background reduction as it is explicitly described in [13]. Briefly, the high resolution of our spectrometer allows separating the Si RRS-KL [15] structure, which is usually the limiting factor for the detection limit of Al and whose edge depends directly on the primary beam energy, from the Al-Kα fluorescence line by choosing an energy just above the Al K-edge. This separation is not possible with energy dispersive detectors due to their lower resolution. Finally, only the weak Si RRS-KM and the elec-

tric noise of the CCD overlap with Al-Kα line. A direct detection limit of $4 * 10^{12}$ for Al was achieved with these optimized background conditions for the detection of Al [16].

Angular dependant scans were performed by means of an automated acquisition system for each implanted sample for both, the Si-Kα and the Al-Kα fluorescence lines. The Al-Kα was measured twice at 100 different positions separated by 0.02250° for 50 seconds, afterwards the two scans were added. These two successive scans allowed us checking the reproducibility of our system which was found to be excellent. The Si-Kα was measured at 40 different points separated by 0.05625° for 20 seconds. The latter angular dependant profile was needed for calibration reasons. In fact the exit angle cannot be controlled on an absolute scale but only on a relative scale since only the change in exit angle can be fixed. In order to know the exit angle on an absolute scale a reference position is needed which is in our case the critical angle of the Si-Kα line of the considered sample. Once this reference position is known and the offset of our setup fixed, the absolute exit angle can be determined for every target position of the considered sample.

In total nine different Al-implanted samples were analyzed, the implantation energies being 1 keV, 5 keV, 10 keV, 15 keV, 20 keV, 25 keV, 30 keV, 50 keV, 100 keV. Each implantation was realized at room temperature and 90° incidence to the surface with a flux of 10^{16} at/cm^2 into clean Si (100) wafers with a thickness of 0.2 mm. The implantations with energies between 1 keV and 30 keV were realized at the Ion Beam Physics and Materials Research Institute at the Forschungszentrum Dresden-Rossendorf in Germany, the two other ones were realized at the Institute of Electronic Materials Technology in Warsaw, Poland. The motivation to focus on lower implantation energies is given by the already mentioned device scaling. The upper implantation energies were chosen to see the limits of our setup. The critical angle of the Si-Kα line for the implanted sample was considered to be the same as for bulk Si. This procedure justified by the fact that the implanted dose is too low to induce significant changes in the refractive index. Indeed, for the discussed samples, the most significant changes are expected for the lowest implantation energy since it presents the highest peak concentration of Al. Calculations predict that the maximum relative change (at the peak position of the implant realized with 1 keV) of the real part of the refractive index describing the scattering properties is of the order of 10^{-6} whereas for the imaginary part describing the absorption properties it is about 4%. These small changes are also due to the fact that two neighbouring elements in the

periodic table are considered.

4. Results

The distribution of the implanted ions was first theoretically calculated by means of the TRIM (Transport and Range of Ions in Matter) [17] program which is a Monte Carlo simulation of the implantation process taking into account different physical effects. The obtained distributions, covering mean implantation ranges between 3 nm and 180 nm, were then used to calculate theoretical angular profiles by using the equations of [18] modified for the case of ion implanted samples,

$$I(\theta) = |t_0|^2 \int_{z_1}^{z_0} N(z) * e^{-2\mathrm{Im}(k_z)(z_0-z)} * |\text{Multiple reflections}|^2 \, \mathrm{d}z. \qquad (1)$$

$N(z)$ stands for the calculated depth distribution of the implanted ions, t_0 for the transmission factor of the emitted x-rays at the sample-vacuum interface, the exponential corresponds to the absorption of x-rays, $k_z = 2\pi/\lambda * \sqrt{n2 - \cos 2\theta}$, n being the complex refractive index, z_0 the surface of the sample, the z-direction being perpendicular to the surface. Multiple reflections can be neglected since there are no sharp interfaces inside the sample as for layer-like samples. As one can guess in figure 3, where some calculated profiles are compared to measured ones and a nice agreement is found, the theoretical angular profiles change gradually with the depth distribution of the implanted ions. For samples implanted at low energies, a considerable part of the implanted ions is sitting close to the surface which explains the increasing intensity at exit angles even below the critical angle. The extinction depth below the critical angle (see figure 1) is about 3 nm. In addition it can be observed that the critical angle shifts towards larger values with increasing implantation energies. Since the critical angle depends on the surface density of the sample, this corresponds to an illustration of how the number of Al ions sitting close to the surface diminishes wtih increasing implanation energies. In fact the shift tends to the value of the critical angle emitted from pure Si for the energy of the Al-Kα line. Finally the intensity for exit angles much larger than the critical angle depends mainly on the implanted dose, i.e. the number of implanted ions.

Finally, the aim is to extract from the measured angular profiles the depth distribution of the Al ions. Basically this corresponds to an inversion of equation 1 which is not an easy task at all [19]. Therefore a more direct approach

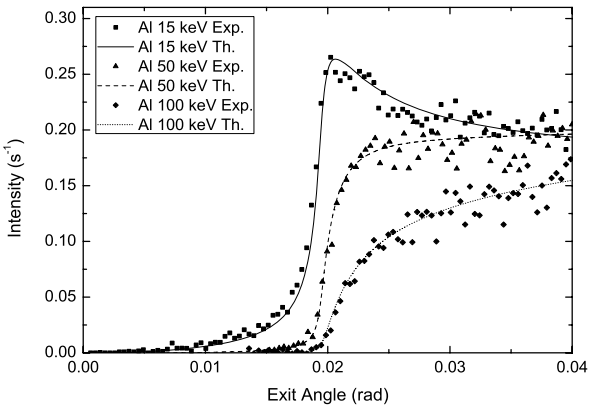

Figure 3: Comparison for some samples between the with equation 1 and the TRIM output theoretically calculated angular profiles with the corresponding experimental results. A good agreement is observed for the shown samples.

will be followed here. Since the shape of implanted ion distributions (Gaussians, Pearson IV distributions, half-joined Gaussians,...) [20] is more or less known from calculations or other experimental results, a known analytical function $N(z)$ will be assumed beforehand to fit the experimental angular profiles with equation 1. We used Gaussians for the fit, the centre and the width of the Gaussian being the free parameters. Indeed, for the present samples, the theoretical depth profiles could be well fitted by Gaussians, Pearson IV distributions did not improve the quality of the fit significantly. As the skewness and the kurtosis of the Pearson IV distributions were close to 0 respectively 3, Gaussian distributions can be safely used since for these values of the skewness and the kurtosis, Pearson IV and Gaussian distributions are identical. Using a Gaussian presents in addition the advantage that there are less free parameters (two instead of four) in the fitting procedure. Note also that for Gaussians distributions which are symmetric, the position of the peak and the mean value of the implantation depth of the ions, the so-called projected range, are identical.

However, the result of the fit of the experimental angular profile depends on the starting values for the centre and the width of the assumed Gaussian distribution. To elude this dependancy the fit was repeated 1000 times, each one with different, randomly scattered starting values for the centre and the width. Afterwards the mean or centre of gravity of all the returned

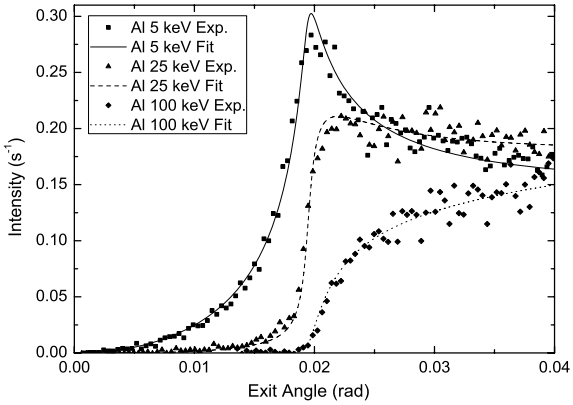

Figure 4: Examples for some of the measured samples of how well the experimental data is fitted by assuming a Gaussian distribution in equation 1 for the implanted ions. Thus, the choice of a Gaussian distribution seems to be justified.

results was taken as the final result for the centre respectively the width of the Gaussian distribution. This procedure allows avoiding staying stuck in local minima. The results of this procedure are shown in 1. In addition the evolution with the number of fits of the correlation coefficient between the experimental angular profile and the profile calculated with the mean values of the realized fits was considered. After 40 to 50 fits it was already converging to the final value and did not change considerably afterwards.

In order to have a complete depth profile, the quantification problem needs also to be addressed since not only the distribution of the implanted ions is of interest but also their number. In this purpose the Al-Kα intensity of an Al bulk sample was measured at a fixed exit angle above the critical angle, in order to compare it to the Al-Kα intensity of the Al-implanted samples at the same exit angle. By correcting this intensity ratio of the Al-Kα lines for the differences in absorption of the primary beam in Si respectively Al and the, due to the grazing exit angle quite pronounced, self-absorption of the Al-Kα inside the considered sample, one can deduce the number of implanted ions, respectively the implantation dose ϕ since

$$\phi = \int_0^T C(x)\mathrm{d}x. \tag{2}$$

where $C(x)$ stands for the dopant distribution deduced from the fitting pro-

E_{Impl}	C_{TRIM}	C_{Fit}	$\sigma_{C_{\mathrm{Fit}}}$	W_{TRIM}	W_{Fit}	$\sigma_{W_{\mathrm{Fit}}}$	ϕ
1 keV	3.65	4.01	0.49	1.92	1.92	0.03	N.A.
5 keV	10.9	9.34	0.15	5.73	5.67	0.03	N.A.
10 keV	18.7	18.3	0.22	9.57	9.53	0.03	N.A.
15 keV	26.1	23.1	0.22	12.6	12.4	0.03	N.A.
20 keV	34.2	32.7	0.37	16.6	16.5	0.03	N.A.
25 keV	42.3	43.4	0.41	19.5	19.6	0.06	N.A.
30 keV	50.2	56.8	0.56	23.4	24.1	0.07	N.A.
50 keV	83.7	82.1	0.38	35.6	35.3	0.06	N.A.
100 keV	173	169	0.67	62.0	61.0	0.17	N.A.

Table 1: Values of the experimentally extracted depth profiles. C stands for the center and W for the width (both in units of nm) of the distribution in the depth direction, whereas ϕ stands for the implantation flux in atoms/cm^2. The experimental results are also compared to the values calculated with the TRIM software.

cedure in atoms per cm^3 and T for the sample thickness. The experimentally deduced implantation dose is also shown in table 1.

5. Discussion

In table 1 the experimentally extracted results for the depth distribution of the Al ions are compared to the values of the theoretical TRIM calculation. A graphical comparison can also be found for some of the samples in figure 5. It can be observed that in most cases the theoretical values for the centre of the distribution are slightly larger than the experimental values. Nevertheless, even if there is not a perfect agreement, the values are quite close showing that the presented high-resolution grazing emission setup is able to distinguish accurately between samples implanted with different energies since the mean implantation depth depends on the initial kinetic energy of the ions. Assuming that the relationship between the mean penetration range of the ions and the implantation energy is correct, the experimentally deduced mean peak positions allow estimating the implantation energy. The values obtained this way are within 10% of the assumed implantation energy except for the sample implanted with 1 keV, but should only be considered as estimates since they are based on theoretical calculations.

Considering the widths of the implanted Al distributions, a really excellent agreement between theoretical and experimental results can be noticed. The results are within 0.3 nm except for the last sample where the x-ray absorption due to Si is more pronounced and, in addition, the real shape of the

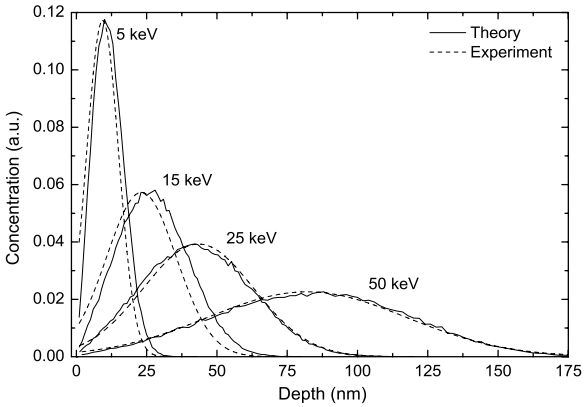

Figure 5: Comparison for some implantation energies of the experimentally deduced depth profiles of the implanted Al ions to the theoretically calculated profiles with TRIM.

implantation profile is a bit distorted towards larger depths as it is usual for increasing implantation energies. Here a fit with a Pearson IV distribution could provide better results. Finally the experimentally deduced shape of the Al ion distribution agrees with the theoretically calculated one, except for the mentioned shift of the peak position of the distribution (see figure 5). This shift may be explained by uncertainties on the parameters used in calculations but also experimental effects in the sample preparation and production cannot be excluded. In table 1 $\sigma_{C_{\mathrm{Fit}}}$ respectively $\sigma_{W_{\mathrm{Fit}}}$ stand for the standard deviation of the distribution of the results returned by the fits for the considered sample. The small values of the standard deviation indicate that the presented high-resolution grazing emission setup allows getting precise results since the dependancy of tha angular profile on the implanted ion distribution seems to be quite pronounced. Only the central peak position of the sample implanted with 1 keV was not so precisely extracted because the results returned by the individual fits were spread on a larger range than it was the case for other samples. Looking closer at some of these results it turned out that the values returned did not fit the angular profile accurately and were thus obviously not consistent. The final result could be improved by rejecting those results. This could be done by requiring a minimum value for the correlation coefficient in the fitting procedure.

paragraph about the results of the quantification procedure....

6. Conclusion

Finally it can be stated that the presented synchrotron radiation based high-resolution GEXRF technique is a great tool for extracting depth profiles in applications where ion implantation is used. In the present case the shape and the location as well as the amount of implanted ions could be quite accurately determined from experimental angular profiles and showed a good agreement with theoretical calculations. Some reasonable a priori knowledge about the shape of the depth distributions needed to be used in the analysis to facilitate the fitting procedure of the angular profiles. It should also be mentioned that Al was chosen as an implant in Si since for this combination the measurements are the most challenging due to the Si background overlapping with the Al signal. Of course it is also possible to perform depth profile measurements with other, more commonly used materials in the semiconductor ion implantation domain, like B and P. To assess the limits of our setup for the extraction of depth profiles a comparison like in [21] would be useful.

The financial support of the Swiss National Foundation is acknowledged. The authors would also like to thank the ESRF for supporting this experiment.

References

[1] C. B. Yarling, History of industrial and commercial ion implantation, J. Vac. Sci. Technol. A, Vol. 18 (2000), Issue 4, 1746-1750.

[2] Iwaki, M., Progress in ion implantation technology for metal surface treatments and other related topics, International Conference on Ion Implantation Technology Proceedings, 1998, Vol. 2, 824-826.

[3] J. M. Poate and L. Rubin, Ion Implantation in Silicon Technology, Ind. Phys. 9 (2003), 12-15.

[4] Z.M. Spolnik et al., Quantification in grazing-emission x-ray fluorescence spectrometry, Spectrochim. Acta Part B 54, 1525-1537 (1999).

[5] A. Kuczumow et al., Quantification problems in ligth element determination by grazing emission x-ray fluorescence, J. Anal. At. Spectrom. 25, 415-421 (2000).

[6] R. Klockenkämper et al., Determination of the implantation dose in silicon wafers by x-ray fluorescence analysis, Anal. Chem 62, 1674-1676 (1990).

[7] R. Klockenkämper and A. von Bohlen, A new method for method for depth-profiling of shallow layers in silicon wafers by repeated chemical etching and total-reflection X-ray fluorescence analysis, Spectrochim. Acta Part B 54, 1385-1392 (1999).

[8] R. Klockenkämper, Total Reflection X-Ray Fluorescence Analysis (Wiley, New York, 1997).

[9] R.S. Becker, J.A. Golovchenko and J.R. Patel, X-ray Evanescent Wave Absorption and Emission, Phys. Rev. Lett. 50, 1858 - 1861 (1983).

[10] P.K. de Bokx et al., Grazing-emission x-ray fluorescence spectrometry: principles and applications, Spectrochim. Acta Part B 52, 829-840 (1997).

[11] C.Streli et al., Analysis of low Z elements on Si wafer surfaces with undulator radiation induced total reflection X-ray fluorescence at the PTB beamline at BESSY II, Spectrochim. Acta Part B 58, 2113-2121 (2003).

[12] J. Hoszowska, J. -Cl. Dousse, J. Kern, and Ch. Rhême, Nucl. Instrum. Methods Phys. Res. A 376, 129 (1996).

[13] J. Szlachetko et al., Application of the high-resolution grazing-emission x-ray fluorescence method for impurities control in semiconductor nantechnology, J. Appl. Phys. 105, 086101 (2009).

[14] M. Claes et al., Progress in laboratory grazing-emission x-ray fluorescence spectrometry, X-Ray Spectrom. 28, 224-229 (1999).

[15] J. Szlachetko et al., High-resolution study of x-ray resonant Raman scattering at the K edge of silicon, Phys. Rev. Lett. 97, 073001 (2006).

[16] A. Kubala-Kukus et al., Observation of ultra low-level Al-impurities on silicon surface by high-resolution grazing emission x-ray fluorescence excited by synchrotron radiation,...

[17] J.F. Ziegler et al., The stopping and range of ions in solids, Pergamon Press, New York, 1985.

[18] H. P. Urbach and P. K. de Bokx, Grazing emission x-ray fluorescence from multilayers, Phys. Rev. B 63, 085408 (2001).

[19] C. Kok and H.P. Urbach, On the regularization of the inverse Laplace transform in grazing-emission x-ray fluorescence spectroscopy, Inverse Problems in Engineering, Vol. 7 (1999), 433-470.

[20] K. Suzuki et al., Comprehensive analytical expression for dose dependent ion-implanted impurity concentration profiles, Solid-State Electronics 42, 1671-1678 (1998).

[21] R. Klockenkämper et al., Depth profiles of a shallow implanted layer in a Si wafer determined by different methods of thin-layer analysis, Spectrochim Acta Part B 57, 1593-1599 (2002).